



VIBRATIONAL MODES OF CARBON NANOTUBES; SPECTROSCOPY AND THEORY

P. C. EKLUND,¹ J. M. HOLDEN,¹ and R. A. JISHI²

¹Department of Physics and Astronomy and Center for Applied Energy Research,
University of Kentucky, Lexington, KY 40506, U.S.A.

²Department of Physics, Massachusetts Institute of Technology, Cambridge, MA 02139, U.S.A.;
Department of Physics, California State University, Los Angeles, CA 90032, U.S.A.

(Received 9 February 1995; accepted in revised form 21 February 1995)

Abstract—Experimental and theoretical studies of the vibrational modes of carbon nanotubes are reviewed. The closing of a 2D graphene sheet into a tubule is found to lead to several new infrared (IR)- and Raman-active modes. The number of these modes is found to depend on the tubule symmetry and not on the diameter. Their diameter-dependent frequencies are calculated using a zone-folding model. Results of Raman scattering studies on arc-derived carbons containing nested or single-wall nanotubes are discussed. They are compared to theory and to that observed for other sp^2 carbons also present in the sample.

Key Words—Vibrations, infrared, Raman, disordered carbons, carbon nanotubes, normal modes.

1. INTRODUCTION

In this paper, we review progress in the experimental detection and theoretical modeling of the normal modes of vibration of carbon nanotubes. Insofar as the theoretical calculations are concerned, a carbon nanotube is assumed to be an infinitely long cylinder with a monolayer of hexagonally ordered carbon atoms in the tube wall. A carbon nanotube is, therefore, a one-dimensional system in which the cyclic boundary condition around the tube wall, as well as the periodic structure along the tube axis, determine the degeneracies and symmetry classes of the one-dimensional vibrational branches [1–3] and the electronic energy bands[4–12].

Nanotube samples synthesized in the laboratory are typically not this perfect, which has led to some confusion in the interpretation of the experimental vibrational spectra. Unfortunately, other carbonaceous material (e.g., graphitic carbons, carbon nanoparticles, and amorphous carbon coatings on the tubules) are also generally present in the samples, and this material may contribute artifacts to the vibrational spectrum. Defects in the wall (e.g., the inclusion of pentagons and heptagons) should also lead to disorder-induced features in the spectra. Samples containing concentric, coaxial, “nested” nanotubes with inner diameters ~8 nm and outer diameters ~80 nm have been synthesized using carbon arc methods[13,14], combustion flames[15], and using small Ni or Co catalytic particles in hydrocarbon vapors[16–20]. Single-wall nanotubes (diameter 1–2 nm) have been synthesized by adding metal catalysts to the carbon electrodes in a dc arc[21,22]. To date, several Raman scattering studies[23–28] of nested and single-wall carbon nanotube samples have appeared.

2. OVERVIEW OF RAMAN SCATTERING FROM SP^2 CARBONS

Because a single carbon nanotube may be thought of as a graphene sheet rolled up to form a tube, carbon nanotubes should be expected to have many properties derived from the energy bands and lattice dynamics of graphite. For the very smallest tubule diameters, however, one might anticipate new effects stemming from the curvature of the tube wall and the closing of the graphene sheet into a cylinder. A natural starting point for the discussion of the vibrational modes of carbon nanotubes is, therefore, an overview of the vibrational properties of sp^2 carbons, including carbon nanoparticles, disordered sp^2 carbon, and graphite. This is also important because these forms of carbon are also often present in tubule samples as “impurity phases.”

In Fig. 1a, the phonon dispersion relations for 3D graphite calculated from a Born-von Karman lattice-dynamical model are plotted along the high symmetry directions of the Brillouin zone (BZ). For comparison, we show, in Fig. 1b, the results of a similar calculation[29] for a 2D infinite graphene sheet. Interactions up to fourth nearest neighbors were considered, and the force constants were adjusted to fit relevant experimental data in both of these calculations. Note that there is little dispersion in the k_z (Γ to A) direction due to the weak interplanar interaction in 3D graphite (Fig. 1c). To the right of each dispersion plot is the calculated one-phonon density of states. On the energy scale of these plots, very little difference is detected between the structure of the 2D and 3D one-phonon density of states. This is due to the weak interplanar coupling in graphite. The eigenvectors for the optically

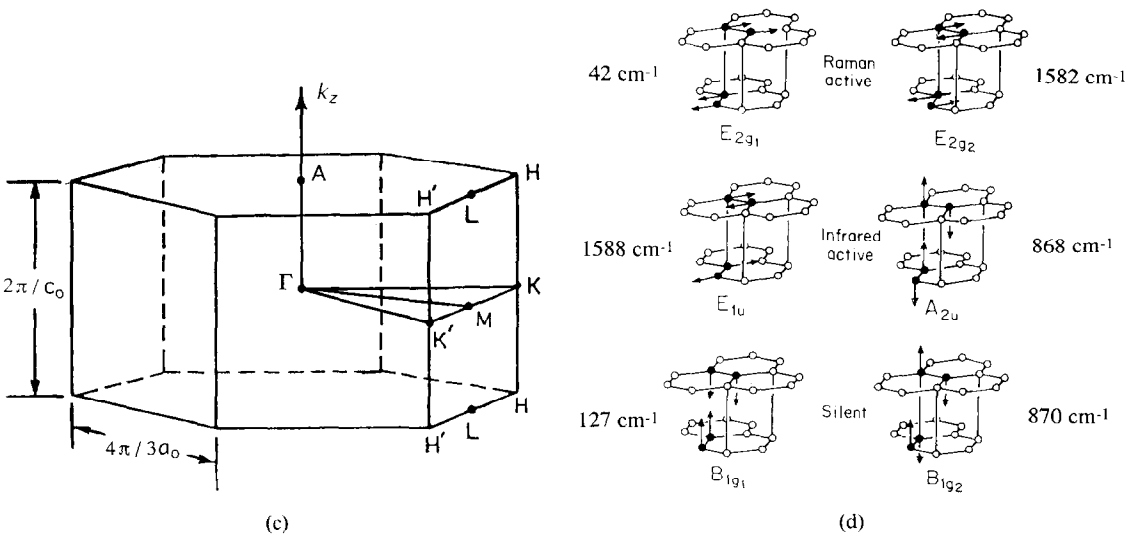
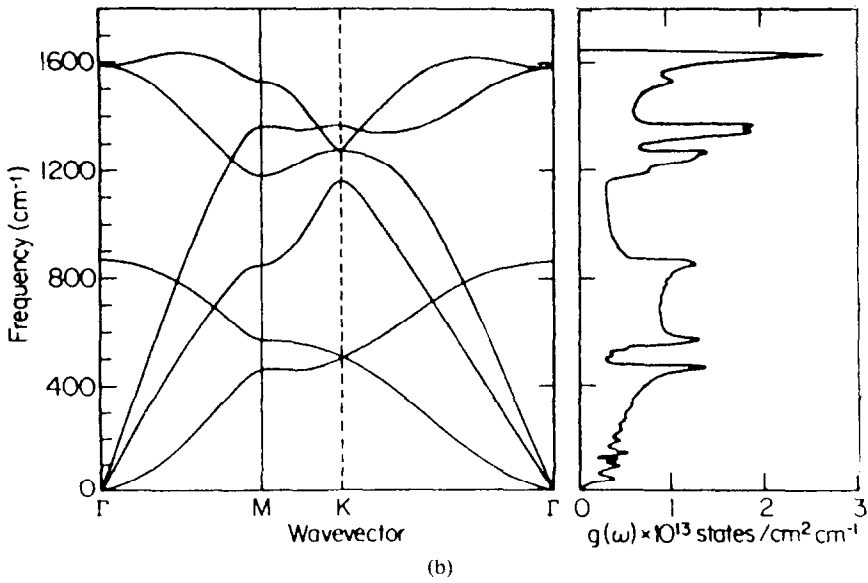
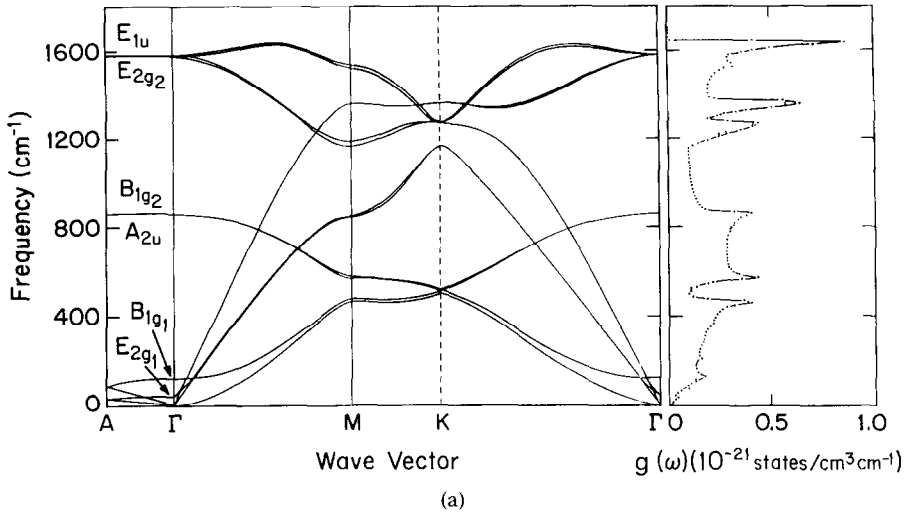


Fig. 1. Phonon modes in 2D and 3D graphite: (a) 3D phonon dispersion, (b) 2D phonon dispersion, (c) 3D Brillouin zone, (d) zone center $q = 0$ modes for 3D graphite.

allowed Γ -point vibrations for graphite (3D) are shown in Fig. 1d, which consist of two, doubly degenerate, Raman-active modes ($E_{2g}^{(1)}$ at 42 cm^{-1} , $E_{2g}^{(2)}$ at 1582 cm^{-1}), a doubly degenerate, infrared-active E_{1u} mode at 1588 cm^{-1} , a nondegenerate, infrared-active A_{2u} mode at 868 cm^{-1} , and two doubly degenerate B_{2g} modes (127 cm^{-1} , 870 cm^{-1}) that are neither Raman- nor infrared-active. The lower frequency $B_{2g}^{(1)}$ mode has been observed by neutron scattering, and the other is predicted at 870 cm^{-1} . Note the Γ -point E_{1u} and $E_{2g}^{(2)}$ modes have the same intralayer motion, but differ in the relative phase of their C-atom displacements in adjacent layers. Thus, it is seen that the interlayer interaction in graphite induces only an $\sim 6\text{ cm}^{-1}$ splitting between these modes ($\omega(E_{1u}) - \omega(E_{2g}^{(2)}) = 6\text{ cm}^{-1}$). Furthermore, the frequency of the rigid-layer, shear mode ($\omega(E_{2g}^{(1)}) = 42\text{ cm}^{-1}$) provides a second spectroscopic measure of the interlayer interaction because, in the limit of zero interlayer coupling, we must have $\omega(E_{2g}^{(1)}) \rightarrow 0$.

The Raman spectrum ($300\text{ cm}^{-1} \leq \omega \leq 3300\text{ cm}^{-1}$) for highly oriented pyrolytic graphite (HOPG)¹ is shown in Fig. 2a, together with spectra (Fig. 2b–e) for several other forms of sp^2 bonded carbons with varying degrees of intralayer and interlayer disorder. For HOPG, a sharp first-order line at 1582 cm^{-1} is observed, corresponding to the Raman-active $E_{2g}^{(2)}$ mode observed in single crystal graphite at the same frequency[31]. The first- and second-order mode frequencies of graphite, disordered sp^2 carbons and carbon nanotubes, are collected in Table 1.

Graphite exhibits strong second-order Raman-active features. These features are expected and observed in carbon tubules, as well. Momentum and energy conservation, and the phonon density of states determine, to a large extent, the second-order spectra. By conservation of energy: $\hbar\omega = \hbar\omega_1 + \hbar\omega_2$, where ω and ω_i ($i = 1, 2$) are, respectively, the frequencies of the incoming photon and those of the simultaneously excited normal modes. There is also a crystal momentum selection rule: $\hbar\mathbf{k} = \hbar\mathbf{q}_1 + \hbar\mathbf{q}_2$, where \mathbf{k} and \mathbf{q}_i ($i = 1, 2$) are, respectively, the wavevectors of the incoming photon and the two simultaneously excited normal modes. Because $\mathbf{k} \ll \mathbf{q}_B$, where \mathbf{q}_B is a typical wavevector on the boundary of the BZ, it follows that $\mathbf{q}_1 \approx -\mathbf{q}_2$. For a second-order process, the strength of the IR lattice absorption or Raman scattering is proportional to $|M(\omega)|^2 g_2(\omega)$, where $g_2(\omega) = g_1(\omega_1) \cdot g_1(\omega_2)$ is the two-phonon density of states subject to the condition that $\mathbf{q}_1 = -\mathbf{q}_2$, and where $g_1(\omega)$ is the one-phonon density of states and $|M(\omega)|^2$ is the effective two-phonon Raman matrix element. In covalently bonded solids, the second-order spectral features are generally broad, consistent with the strong dispersion (or wide bandwidth) of both the optical and acoustic phonon branches.

However, in graphite, consistent with the weak interlayer interaction, the phonon dispersion parallel to

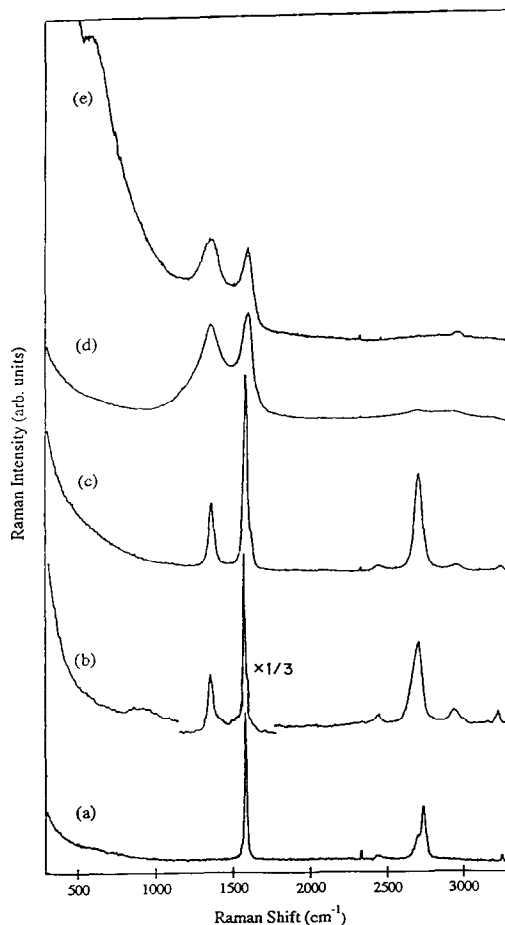


Fig. 2. Raman spectra ($T = 300\text{ K}$) from various sp^2 carbons using Ar-ion laser excitation: (a) highly ordered pyrolytic graphite (HOPG), (b) boron-doped pyrolytic graphite (BHOPG), (c) carbon nanoparticles (dia. 20 nm) derived from the pyrolysis of benzene and graphitized at 2820°C , (d) as-synthesized carbon nanoparticles ($\sim 850^\circ\text{C}$), (e) glassy carbon (after ref. [24]).

the c-axis (i.e., along the k_z direction) is small. Also, there is little in-plane dispersion of the optic branches and acoustic branches near the zone corners and edges (M to K). This low dispersion enhances the peaks in the one-phonon density of states, $g_1(\omega)$ (Fig. 1a). Therefore, relatively sharp second-order features are observed in the Raman spectrum of graphite, which correspond to characteristic combination ($\omega_1 + \omega_2$) and overtone (2ω) frequencies associated with these low-dispersion (high one-phonon density of states) regions in the BZ. For example, a second-order Raman feature is detected at 3248 cm^{-1} , which is close to $2(1582\text{ cm}^{-1}) = 3164\text{ cm}^{-1}$, but significantly upshifted due to the 3D dispersion of the uppermost phonon branch in graphite. The most prominent feature in the graphite second-order spectrum is a peak close to $2(1360\text{ cm}^{-1}) = 2720\text{ cm}^{-1}$ with a shoulder at 2698 cm^{-1} , where the lineshape reflects the density of two-phonon states in 3D graphite. Similarly, for a 2D graphene sheet, in-plane dispersion (Fig. 1b) of the optic branches at the zone center and in the acoustic

¹HOPG is a synthetic polycrystalline form of graphite produced by Union Carbide[30]. The c-axes of each grain (dia. $\sim 1\text{ }\mu\text{m}$) are aligned to $\sim 1^\circ$.

Table 1. Table of frequencies for graphitic carbons and nanotubes

Mode assignment*† (tube dia.)	Planar graphite		Single-wall tubules			Nested tubules		
	HOPG[31]	BHOPG[31]	Holden‡	Holden	Hiura	Chandrabhas	Bacsa	Kastner
			<i>et al.</i> [27] (1–2 nm)	<i>et al.</i> [28] (1–2 nm)		<i>et al.</i> [24] (15–50 nm)	<i>et al.</i> [26] (8–30 nm)	<i>et al.</i> [25] (20–80 nm)
$E_{2g}^{(1)}$ (R, \perp)	42 ^c					49, 58 ^c		
$B_{2g}^{(1)}$ (S, \parallel)	127 ^h							
A_{2u} (ir, \parallel)	868 ^g	~900 ^c				~700 ^c		868 ^g
$B_{2g}^{(2)}$ (S, \parallel)	870 ⁱ	~900 ^c						
$E_{2g}^{(2)}$ (R, \perp)	1582 ^c 1577 ^c	1585 ^c 1591 ^c	1566 ^{c,d} 1592 ^{c,d}	1568 ^c 1594 ^c	1574 ^a	1583 ^c	1581 ^a	1582 ^c
E_{1u} (ir, \perp)	1588 ^g							1575 ^g
D (R, \perp)	1350 ^c 1365 ^c	1367 ^c 1380 ^c		1341 ^c	1340 ^a	1353 ^c	1356 ^a	varies ^f
E'_{2g} (R, \perp)		1620 ^c						1620 ^a
2×1220 (R, \perp)	2441 ^c	2450 ^c 2440 ^c		2450 ^c	2455 ^a	2455 ^c	2450 ^a	2455 ^c
$2 \times D$ (R, \perp)	2722 ^c 2746 ^c	2722 ^c 2753 ^c	2681 ^{c,d}	2680 ^c	2687 ^a	2709 ^c		2734 ^c
$E_{2g}^{(2)} + D$ (R, \perp)		2950 ^c 2974 ^c		2925 ^c				2925 ^c
$2E'_{2g}$ (R, \perp)	3247 ^c 3246 ^c	3240 ^c 3242 ^c	3180 ^{c,d}	3180 ^c		3250 ^a	3250 ^a	3252 ^c

*Activity: R = Raman-active, ir = infrared-active, S = optically silent, observed in neutron scattering.

†Carbon atom displacement \parallel or \perp to \hat{C} .

‡Peaks in “difference spectrum” (see section 4.3).

^{a–c}Excitation wavelength: ^a742 nm, ^b532 nm, ^c514 nm, ^d488 nm, ^e458 nm; ^f resonance Raman scattering study; ^gir-absorption study; ^hfrom neutron scattering; ⁱpredicted.

branches near the zone corners and edges is weak, giving rise to peaks in the one-phonon density of states. One anticipates, therefore, that similar second-order features will also be observed in carbon nanotubes. This is because the zone folding (c.f., section 4) preserves in the tubule the essential character of the in-plane dispersion of a graphene sheet for \mathbf{q} parallel to the tube axis. However, in small-diameter carbon nanotubes, the cyclic boundary conditions around the tube wall activate many new first-order Raman- and IR-active modes, as discussed below.

Figure 2b shows the Raman spectrum of Boron-doped, highly oriented pyrolytic-graphite (BHOPG) according to Wang *et al.*[32]. Although the BHOPG spectrum is similar to that of HOPG, the effect of the 0.5% substitutional boron doping is to create in-plane disorder, without disrupting the overall AB stacking of the layers or the honeycomb arrangement of the remaining C-atoms in the graphitic planes. However, the boron doping relaxes the $\mathbf{q} \approx 0$ optical selection rule for single-phonon scattering, enhancing the Raman activity of the graphitic one- and two-phonon density of states. Values for the peak frequencies of the first- and second-order bands in BHOPG are tabulated in Table 1. Significant disorder-induced Raman activity in the graphitic one-phonon density of states is observed near 1367 cm^{-1} , similar to that observed in other disordered sp^2 bonded carbons, where features in the range ~1360–1365 cm^{-1} are detected. This band is referred to in the literature as the “D-band,” and the position of this band has been shown to de-

pend weakly on the laser excitation wavelength[32]. This unusual effect arises from a resonant coupling of the excitation laser with electronic states associated with the disordered graphitic material. Small basal plane crystallite size (L_a) has also been shown[33] to activate disorder-induced scattering in the D-band. The high frequency $E_{2g}^{(2)}$ ($q = 0$) mode has also been investigated in a wide variety of graphitic materials that have various degrees of in-plane and stacking disorder[32]. The frequency, strength, and line-width of this mode is also found to be a function of the degree of the disorder, but the peak position depends much less strongly on the excitation frequency.

The Raman spectrum of a strongly disordered sp^2 carbon material, “glassy” carbon, is shown in Fig. 2e. The $E_{2g}^{(2)}$ -derived band is observed at 1600 cm^{-1} and is broadened along with the D-band at 1359 cm^{-1} . The similarity of the spectrum of glassy carbon (Fig. 2e) to the one-phonon density of states of graphite (Fig. 1a) is apparent, indicating that despite the disorder, there is still a significant degree of sp^2 short-range order in the glassy carbon. The strongest second-order feature is located at 2973 cm^{-1} , near a combination band ($\omega_1 + \omega_2$) expected in graphite at D (1359 cm^{-1}) + E'_{2g} (1620 cm^{-1}) = 2979 cm^{-1} , where the E'_{2g} (1620 cm^{-1}) frequency is associated with a mid-zone maximum of the uppermost optical branch in graphite (Fig. 1a).

The carbon black studied here was prepared by a CO_2 laser-driven pyrolysis of a mixture of benzene, ethylene, and iron carbonyl[34]. As synthesized, TEM

images show that this carbon nanosoot consists of disordered sp^2 carbon particles with an average particle diameter of ~ 200 Å. The Raman spectrum (Fig. 2d) of the “as synthesized” carbon black is very similar to that of glassy carbon (Fig. 2e) and has broad disorder-induced peaks in the first-order Raman spectrum at 1359 and 1600 cm^{-1} , and a broad second-order feature near 2950 cm^{-1} . Additional weak features are observed in the second-order spectrum at 2711 and 3200 cm^{-1} , similar to values in HOPG, but appearing closer to $2(1359$ $\text{cm}^{-1}) = 2718$ cm^{-1} and $2(1600$ $\text{cm}^{-1}) = 3200$ cm^{-1} , indicative of somewhat weaker 3D phonon dispersion, perhaps due to weaker coupling between planes in the nanoparticles than found in HOPG. TEM images[34] show that the heat treatment of the laser pyrolysis-derived carbon nanosoot to a temperature $T_{HT} = 2820^\circ\text{C}$ graphitizes the nanoparticles (i.e., carbon layers spaced by ~ 3.5 Å are aligned parallel to facets on hollow polygonal particles). As indicated in Fig. 2c, the Raman spectrum of this heat-treated carbon black is much more “graphitic” (similar to Fig. 2a) and, therefore, a decrease in the integrated intensity of the disorder-induced band at 1360 cm^{-1} and a narrowing of the 1580 cm^{-1} band is observed. Note that heat treatment allows a shoulder associated with a maximum in the mid-BZ density of states to be resolved at 1620 cm^{-1} , and dramatically enhances and sharpens the second-order features.

3. THEORY OF VIBRATIONS IN CARBON NANOTUBES

A single-wall carbon nanotube can be visualized by referring to Fig. 3, which shows a 2D graphene sheet with lattice vectors \mathbf{a}_1 and \mathbf{a}_2 , and a vector \mathbf{C} given by

$$\mathbf{C} = n\mathbf{a}_1 + m\mathbf{a}_2, \quad (1)$$

where n and m are integers. By rolling the sheet such that the tip and tail of \mathbf{C} coincide, a cylindrical nano-

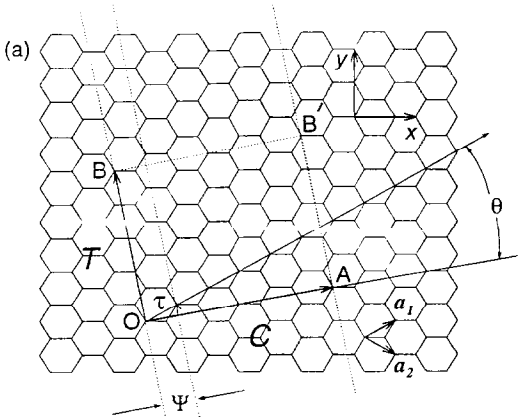


Fig. 3. Translation vectors used to define the symmetry of a carbon nanotube (see text). The vectors \mathbf{a}_1 and \mathbf{a}_2 define the 2D primitive cell.

tube specified by (n, m) is obtained. If $n = m$, the resulting nanotube is referred to as an “armchair” tubule, while if $n = 0$ or $m = 0$, it is referred to as a “zigzag” tubule; otherwise ($n \neq m \neq 0$) it is known as a “chiral” tubule. There is no loss of generality if it is assumed that $n > m$.

The electronic properties of single-walled carbon nanotubes have been studied theoretically using different methods[4-12]. It is found that if $n - m$ is a multiple of 3, the nanotube will be metallic; otherwise, it will exhibit a semiconducting behavior. Calculations on a 2D array of identical armchair nanotubes with parallel tube axes within the local density approximation framework indicate that a crystal with a hexagonal packing of the tubes is most stable, and that intertubule interactions render the system semiconducting with a zero energy gap[35].

3.1 Symmetry groups of nanotubes

A cylindrical carbon nanotube, specified by (n, m) , can be considered a one-dimensional crystal with a fundamental lattice vector \mathbf{T} , along the direction of the tube axis, of length given by[1,3]

$$T = \sqrt{3}C/d_R \quad (2)$$

where

$$\begin{aligned} d_R &= d \quad \text{if } n - m \neq 3d \\ &= 3d \quad \text{if } n - m = 3d \end{aligned} \quad (3)$$

where C is the length of the vector in eqn (1), d is the greatest common divisor of n and m , and r is any integer. The number of atoms per unit cell is $2N$ such that

$$N = 2(n^2 + m^2 + nm)/d_R. \quad (4)$$

For a chiral nanotube specified by (n, m) , the cylinder is divided into d identical sections; consequently a rotation about the tube axis by the angle $2\pi/d$ constitutes a symmetry operation. Another symmetry operation, $R = (\psi, \tau)$ consists of a rotation by an angle ψ given by

$$\psi = 2\pi \frac{\Omega}{Nd} \quad (5)$$

followed by a translation τ , along the direction of the tube axis, given by

$$\tau = \mathbf{T} \frac{d}{N}. \quad (6)$$

The quantity Ω that appears in eqn (5) is expressed in terms of n and m by the relation

$$\Omega = \{p(m + 2n) + q(n + 2m)\} (d/d_R) \quad (7)$$

where p and q are integers that are uniquely determined by the eqn

$$mp - nq = d, \quad (8)$$

subject to the conditions $q < m/d$ and $p < n/d$.

For the case $d = 1$, the symmetry group of a chiral nanotube specified by (n, m) is a cyclic group of order N given by

$$\mathcal{C}_{N/\Omega} = \{\mathcal{R}_{N/\Omega}, \mathcal{R}_{N/\Omega}^2, \dots, \mathcal{R}_{N/\Omega}^{N-1}, \mathcal{R}_{N/\Omega}^N = E\} \quad (9)$$

where E is the identity element, and $\mathcal{R}_{N/\Omega} = (2\pi(\Omega/N), \mathbf{T}/N)$. For the general case when $d \neq 1$, the cylinder is divided into d equivalent sections. Consequently, it follows that the symmetry group of the nanotube is given by

$$\mathcal{C} = \mathcal{C}_d \otimes \mathcal{C}'_{Nd/\Omega} \quad (10)$$

where

$$\mathcal{C}_d = \{C_d, C_d^2, \dots, C_d^d = E\} \quad (11)$$

and

$$\mathcal{C}'_{Nd/\Omega} = \{\mathcal{R}_{Nd/\Omega}, \mathcal{R}_{Nd/\Omega}^2, \dots, \mathcal{R}_{Nd/\Omega}^{N/d} = E\}. \quad (12)$$

Here the operation \mathcal{C}_d represents a rotation by $2\pi/d$ about the tube axis; the angles of rotation in $\mathcal{C}'_{Nd/\Omega}$ are defined modulo $2\pi/d$, and the symmetry element $\mathcal{R}_{Nd/\Omega} = (2\pi(\Omega/Nd), \mathbf{T}d/N)$.

The irreducible representations of the symmetry group \mathcal{C} are given by $A, B, E_1, E_2, \dots, E_{N/2-1}$. The A representation is completely symmetric, while in the B representation, the characters for the operations C_d and $\mathcal{R}_{Nd/\Omega}$ are

$$\chi(C_d) = +1, \quad (13)$$

and

$$\chi(\mathcal{R}_{Nd/\Omega}) = -1. \quad (14)$$

In the E_n irreducible representation, the character of any symmetry operation corresponding to a rotation by an angle ξ is given by

$$\chi(C) = \begin{cases} e^{i2\pi\xi n} \\ e^{-i2\pi\xi n} \end{cases} \quad (15)$$

Equations (13–15) completely determine the character table of the symmetry group \mathcal{C} for a chiral nanotube.

Applying the above symmetry formulation to armchair ($n = m$) and zigzag ($m = 0$) nanotubes, we find that such nanotubes have a symmetry group given by the product of the cyclic group \mathcal{C}_n and \mathcal{C}'_{2n} , where \mathcal{C}'_{2n} consists of only two symmetry operations: the identity, and a rotation by $2\pi/2n$ about the tube axis followed by a translation by $\mathbf{T}/2$. Armchair and zig-

zag nanotubes, however, have other symmetry operations, such as inversion and reflection in planes parallel to the tube axis. Thus, the symmetry group, assuming an infinitely long nanotube with no caps, is given by

$$\mathcal{C} = \begin{cases} \mathcal{D}_{nd} \otimes \mathcal{C}'_{2n} & n \text{ odd} \\ \mathcal{D}_{nh} \otimes \mathcal{C}'_{2n} & n \text{ even} \end{cases} \quad (16)$$

Thus $\mathcal{C} = \mathcal{D}_{2nh}$ in these cases. The choice of \mathcal{D}_{nd} or \mathcal{D}_{nh} in eqn (16) is made to insure that inversion is a symmetry operation of the nanotube. Even though we neglect the caps in calculating the vibrational frequencies, their existence, nevertheless, reduces the symmetry to either \mathcal{D}_{nd} or \mathcal{D}_{nh} .

Of course, whether the symmetry groups for armchair and zigzag tubules are taken to be \mathcal{D}_{nd} (or \mathcal{D}_{nh}) or \mathcal{D}_{2nh} , the calculated vibrational frequencies will be the same; the symmetry assignments for these modes, however, will be different. It is, thus, expected that modes that are Raman or IR-active under \mathcal{D}_{nd} or \mathcal{D}_{nh} but are optically silent under \mathcal{D}_{2nh} will only show a weak activity resulting from the fact that the existence of caps lowers the symmetry that would exist for a nanotube of infinite length.

3.2 Model calculations of phonon modes

The BZ of a nanotube is a line segment along the tube direction, of length $2\pi/T$. The rectangle formed by vectors \mathbf{C} and \mathbf{T} , in Fig. 3, has an area N times larger than the area of the unit cell of a graphene sheet formed by vectors \mathbf{a}_1 and \mathbf{a}_2 , and gives rise to a rectangular BZ than is N times smaller than the hexagonal BZ of a graphene sheet. Approximate values for the vibrational frequencies of the nanotubes can be obtained from those of a graphene sheet by the method of zone folding, which in this case implies that

$$\omega_{1D}(k; \mu) = \omega_{2D}\left(k\hat{T} + \frac{2\pi\mu}{C}\hat{C}\right), \quad \mu = 0, 1, \dots, N-1. \quad (17)$$

In the above eqn, 1D refers to the nanotubes whereas 2D refers to the graphene sheet, k is the 1D wave vector, and \hat{T} and \hat{C} are unit vectors along the tubule axis and vector \mathbf{C} , respectively, and μ labels the tubule phonon branch.

The phonon frequencies of a 2D graphene sheet, for carbon displacements both parallel and perpendicular to the sheet, are obtained[1] using a Born-Von Karman model similar to that applied successfully to 3D graphite. C-C interactions up to the fourth nearest in-plane neighbors were included. For a 2D graphene sheet, starting from the previously published force-constant model of 3D graphite, we set all the force constants connecting atoms in adjacent layers to zero, and we modified the in-plane force constants slightly to describe accurately the results of electron energy loss

spectroscopic measurements, which yield the phonon dispersion curves along the M direction in the BZ. The dispersion curves are somewhat different near M, and along M-K, than the 2D calculations shown in Fig. 1b. The lattice dynamical model for 3D graphite produces dispersion curves $\omega_i(q)$ that are in good agreement with experimental results from inelastic neutron scattering, Raman scattering, and IR spectroscopy.

The zone-folding scheme has two shortcomings. First, in a 2D graphene sheet, there are three modes with vanishing frequencies as $q \rightarrow 0$; they correspond to two translational modes with in-plane C-atom displacements and one mode with out-of-plane C-atom displacements. Upon rolling the sheet into a cylinder, the translational mode in which atoms move perpendicular to the plane will now correspond to the breathing mode of the cylinder for which the atoms vibrate along the radial direction. This breathing mode has a nonzero frequency, but the value cannot be obtained by zone folding; rather, it must be calculated analytically. The frequency of the breathing mode ω_{rad} is readily calculated and is found to be [1,2]

$$\omega_{\text{rad}} = \frac{3a}{4\sqrt{m_C}r_0} [\phi_r^{(1)} + 6\phi_r^{(2)} + 4\phi_r^{(3)} + 14\phi_r^{(4)}]^{1/2} \quad (18)$$

where $a = 2.46 \text{ \AA}$ is the lattice constant of a graphene sheet, r_0 is the tubule radius, m_C is the mass of a carbon atom, and $\phi_r^{(i)}$ is the bond stretching force constant between an atom and its i^{th} nearest neighbor. It should be noted that the breathing mode frequency is found to be independent of n and m , and that it is inversely proportional to the tubule radius. The value of $\omega_{\text{rad}} = 300 \text{ cm}^{-1}$ for $r_0 = 3.5 \text{ \AA}$, the radius that corresponds to a nanotube capped by a C_{60} hemisphere.

Second, the zone-folding scheme cannot give rise to the two zero-frequency tubule modes that correspond to the translational motion of the atoms in the two directions perpendicular to the tubule axis. That is to say, there are no normal modes in the 2D graphene sheet for which the atomic displacements are such that if the sheet is rolled into a cylinder, these displacements would then correspond to either of the rigid tubule translations in the directions perpendicular to the cylinder axis. To convert these two translational modes into eigenvectors of the tubule dynamical matrix, a perturbation matrix must be added to the dynamical matrix. As will be discussed later, these translational modes transform according to the E_1 irreducible representation; consequently, the perturbation should be constructed so that it will cause a mixing of the E_1 modes, but should have no effect in first order on modes with other symmetries. The perturbation matrix turns out to cause the frequencies of the E_1 modes with lowest frequency to vanish, affecting the other E_1 modes only slightly.

Finally, it should be noted that in the *zone-folding* scheme, the effect of curvature on the force constants has been neglected. We make this approximation un-

der the assumption that the hybridization between the sp^2 and p_z orbitals is small. For example, in the armchair nanotube based on C_{60} , with a diameter of approximately 0.7 nm, the three bond angles are readily calculated and they are found to be 120.00° , 118.35° , and 118.35° . Because the deviation of these angles from 120° is very small, the effect of curvature on the force constants might be expected to be small. Based on a calculation using the semi-empirical interatomic Tersoff potential, Bacsa *et al.* [26,36] estimate considerable mode softening with decreasing diameter. For tubes of diameter greater than ~ 10 nm, however, they predict tube wall curvature has negligible effect on the mode frequencies.

3.3 Raman- and infrared-active modes

The frequencies of the tubule phonon modes at the Γ -point, or BZ center, are obtained from eqn (17) by setting $k = 0$. At this point, we can classify the modes according to the irreducible representations of the symmetry group that describes the nanotube. We begin by showing how the classification works in the case of chiral tubules. The nanotube modes obtained from the zone-folding eqn by setting $\mu = 0$ correspond to the Γ -point modes of the 2D graphene sheet. For these modes, atoms connected by any lattice vector of the 2D sheet have the same displacement. Such atoms, under the symmetry operations of the nanotubes, transform into each other; consequently, the nanotube modes obtained by setting $\mu = 0$ are completely symmetric and they transform according to the A irreducible representation.

Next, we consider the Γ -point nanotube modes obtained by setting $k = 0$ and $\mu = N/2$ in eqn (17). The modes correspond to 2D graphene sheet modes at the point $\mathbf{k} = (N\pi/C)\hat{C}$ in the hexagonal BZ. We consider how such modes transform under the symmetry operations of the groups \mathcal{C}_d and $\mathcal{C}'_{Nd/\Omega}$. Under the action of the symmetry element C_d , an atom in the 2D graphene sheet is carried into another atom separated from it by the vector

$$\mathbf{r}_1 = (n/d)\mathbf{a}_1 + (m/d)\mathbf{a}_2. \quad (19)$$

The displacements of two such atoms at the point $\mathbf{k} = (N\pi/C)\hat{C}$ have a phase difference given by

$$\frac{N}{2} \mathbf{k} \cdot \mathbf{r}_1 = 2\pi(n^2 + m^2 + nm)/(dd_R) \quad (20)$$

which is an integral multiple of 2π . Thus, the displacements of the two atoms are equal and it follows that

$$\chi(C_d) = 1. \quad (21)$$

The symmetry operation $R_{Nd/\Omega}$ carries an atom into another one separated from it by the vector

$$\mathbf{r}_2 = p\mathbf{a}_1 + q\mathbf{a}_2, \quad (22)$$

where p and q are the integers uniquely determined by eqn (8). The atoms in the 2D graphene sheet have displacements, at the point $\mathbf{k} = (N\pi/C)\hat{C}$, that are completely out of phase. This follows from the observation that

$$\left(\frac{N\pi}{C}\hat{C}\right) \cdot \mathbf{r}_2 = \frac{\pi\Omega}{d}, \quad (23)$$

and that Ω/d is an odd integer; consequently

$$\chi(R_{Nd/\Omega}) = -1. \quad (24)$$

From the above, we therefore conclude that the nanotube modes obtained by setting $\mu = N/2$, transform according to the B irreducible representation of the chiral symmetry group \mathcal{C} .

Similarly, it can be shown that the nanotube modes at the Γ -point obtained from the zone-folding eqn by setting $\mu = \eta$, where $0 < \eta < N/2$, transform according to the E_η irreducible representation of the symmetry group \mathcal{C} . Thus, the vibrational modes at the Γ -point of a chiral nanotube can be decomposed according to the following eqn

$$\Gamma^{vib} = 6A + 6B6E_1 + 6E_2 + \dots + 6E_{N/2-1} \quad (25)$$

Modes with A , E_1 , or E_2 symmetry are Raman active, while only A and E_1 modes are infrared active. The A modes are nondegenerate and the E modes are doubly degenerate. According to the discussion in the previous section, two A modes and one of the E_1 modes have vanishing frequencies; consequently, for a chiral nanotube there are 15 Raman- and 9 IR-active modes, the IR-active modes being also Raman-active. It should be noted that the number of Raman- and IR-active modes is independent of the nanotube diameter. For a given chirality, as the diameter of the nanotube increases, the number of phonon modes at the BZ center also increases. Nevertheless, the number of the modes that transform according to the A , E_1 , or E_2 irreducible representations does not change. Since only modes with these symmetries will exhibit optical activity, the number of Raman or IR modes does not increase with increasing diameter. This, perhaps unanticipated, result greatly simplifies the data analysis. The symmetry classification of the phonon modes in armchair and zigzag tubules have been studied in ref. [2,3] under the assumption that the symmetry group of these tubules is isomorphic with either \mathcal{D}_{nd} or \mathcal{D}_{nh} , depending on whether n is odd or even. As noted earlier, if one considers an infinite tubule with no caps, the relevant symmetry group for armchair and zigzag tubules would be the group \mathcal{D}_{2nh} . For armchair tubules described by the \mathcal{D}_{nd} group there are, among others, $3A_{1g}$, $6E_{1g}$, $6E_{2g}$, $2A_{2u}$, and $5E_{1u}$ optically active modes with nonzero frequencies; consequently, there are 15 Raman- and 7 IR-active modes. All zigzag tubules, under \mathcal{D}_{nd} or \mathcal{D}_{nh} symmetry group have, among others, $3A_{1g}$, $6E_{1g}$, $6E_{2g}$, $2A_{2u}$, and $5E_{1u}$ op-

tically active modes with nonzero frequencies; thus there are 15 Raman- and 7 IR-active modes.

3.4 Mode frequency dependence on tubule diameter

In Figs. 4–6, we display the calculated tubule frequencies as a function of tubule diameter. The results are based on the zone-folding model of a 2D graphene sheet, discussed above. IR-active (a) and Raman-active (b) modes appear separately for chiral tubules (Fig. 4), armchair tubules (Fig. 5) and zig-zag tubules (Fig. 6). For the chiral tubules, results for the representative (n, m) , indicated to the left in the figure, are displaced vertically according to their calculated diameter, which is indicated on the right. Similar to modes in a C_{60} molecule, the lower and higher frequency modes are expected, respectively, to have radial and tangential character. By comparison of the model calculation results in Figs. 4–6 for the three tube types (armchair, chiral, and zig-zag) a common general behavior is observed for both the IR-active (a) and Raman-active (b) modes. The highest frequency modes exhibit much less frequency dependence on diameter than the lowest frequency modes. Taking the large-diameter tube frequencies as our reference, we see that the four lowest modes stiffen dramatically ($150\text{--}400\text{ cm}^{-1}$) as the tube diameter approaches $\sim 1\text{ nm}$. Conversely, the modes above $\sim 800\text{ cm}^{-1}$ in the large-diameter tubules are seen to be relatively less sensitive to tube diameter: one Raman-active mode stiffens with increasing tubule diameter (armchair), and a few modes in all the three tube types soften ($100\text{--}200\text{ cm}^{-1}$), with decreasing tube diameter. It should also be noted that, in contrast to armchair and zig-zag tubules, the mode frequencies in chiral tubules are grouped near 850 cm^{-1} and 1590 cm^{-1} .

All carbon nanotube samples studied to date have been undoubtedly composed of tubules with a distribution of diameters and chiralities. Therefore, whether one is referring to nanotube samples comprised of single-wall tubules or nested tubules, the results in Figs. 4–6 indicate one should expect inhomogeneous broadening of the IR- and Raman-active bands, particularly if the range of tube diameter encompasses the 1–2 nm range. Nested tubule samples must have a broad diameter distribution and, so, they should exhibit broader spectral features due to inhomogeneous broadening.

4. SYNTHESIS AND RAMAN SPECTROSCOPY OF CARBON NANOTUBES

We next address selected Raman scattering data collected on nanotubes, both in our laboratory and elsewhere. The particular method of tubule synthesis may also produce other carbonaceous matter that is both difficult to separate from the tubules and also exhibits potentially interfering spectral features. With this in mind, we first digress briefly to discuss synthesis and purification techniques used to prepare nanotube samples.

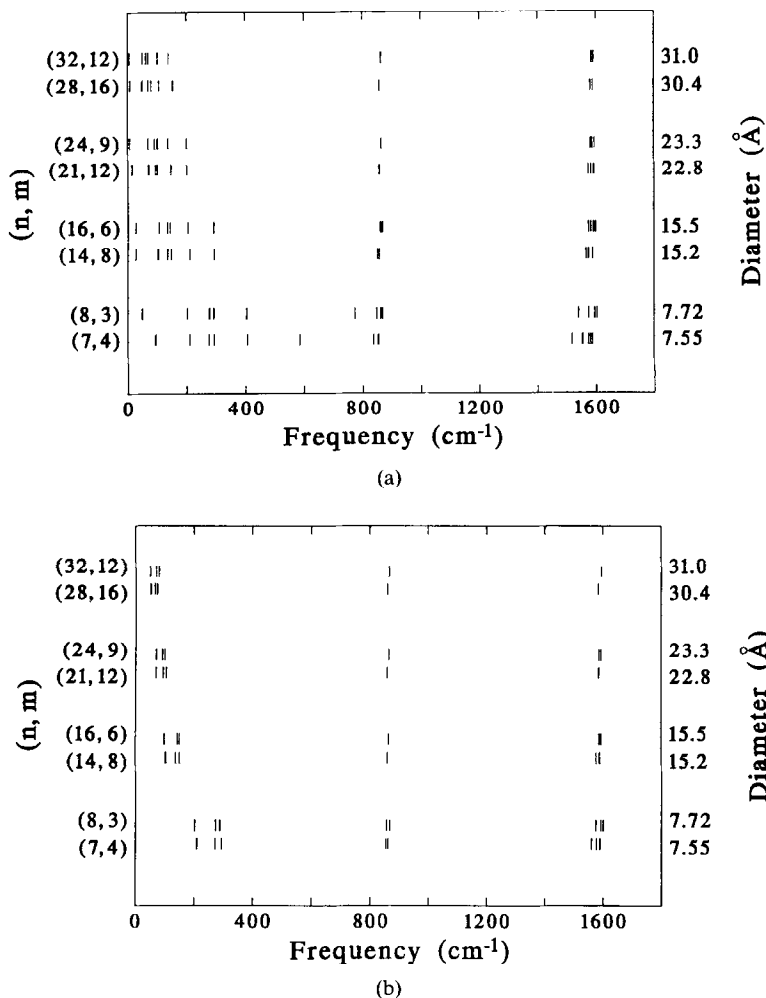


Fig. 4. Diameter dependence of the first order (a) IR-active and, (b) Raman-active mode frequencies for "chiral" nanotubes.

4.1 Synthesis and purification

Nested carbon nanotubes, consisting of closed concentric, cylindrical tubes were first observed by Iijima by TEM[37]. Later TEM studies[38] showed that the tubule ends were capped by the inclusion of pentagons and that the tube walls were separated by ~ 3.4 Å. A dc carbon-arc discharge technique for large-scale synthesis of nested nanotubes was subsequently reported [39]. In this technique, a dc arc is struck between two graphite electrodes under an inert helium atmosphere, as is done in fullerene generation. Carbon vaporized from the anode condenses on the cathode to form a hard, glassy outer core of fused carbon and a soft, black inner core containing a high concentration of nanotubes and nanoparticles. Each nanotube typically contains between 10 and 100 concentric tubes that are grouped in "microbundles" oriented axially within the core[14].

These nested nanotubes may be harvested from the core by grinding and sonication; nevertheless, substantial fractions of other types of carbon remain, all of which are capable of producing strong Raman bands

as discussed in section 2. It is very desirable, therefore, to remove as much of these impurity carbon phases as possible. Successful purification schemes that exploit the greater oxidation resistance of carbon nanotubes have been investigated[40–42]. Thermogravimetric analyses reveal weight loss rate maxima at 420°C, 585°C, and 645°C associated with oxidation (in air) of fullerenes, amorphous carbon soot, and graphite, respectively, to form volatile CO and/or CO₂. Nanotubes and onion-like nanoparticles were found to lose weight rapidly at higher temperatures around 695°C. Evidently, the concentration of these other forms of carbon can be lowered by oxidation. However, the abundant carbon nanoparticles, which are expected to have a Raman spectrum similar to that shown in Figs. 1d or 1c are more difficult to remove in this way. Nevertheless, Ebbesen *et al.* [43] found that, by heating core material to 700°C in air until more than 99% of the starting material had been removed by oxidation, the remaining material consisted solely of open-ended, nested nanotubes. The oxidation was found to initiate at the reactive end caps and progress toward the cen-

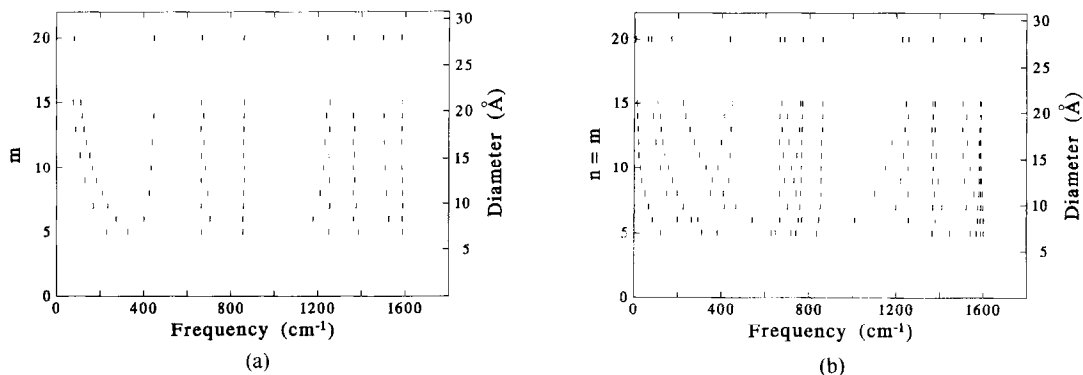


Fig. 5. Diameter dependence of the first order (a) IR-active and, (b) Raman-active mode frequencies for "armchair" nanotubes.

ter only at the open ends[42]. The inner tubules appear to be protected by the outer layers and survive the purification process.

Similar results were found by Bacsa *et al.* [26] for cathode core material. Raman scattering spectra were reported by these authors for material shown in these figures, and these results are discussed below. Their HRTEM images showed that heating core material in air induces a clear reduction in the relative abundance of the carbon nanoparticles. The Raman spectrum of these nanoparticles would be expected to resemble an intermediate between a strongly disordered carbon black synthesized at $\sim 850^\circ\text{C}$ (Fig. 2d) and that of carbon black graphitized in an inert atmosphere at 2820°C (Fig. 2c). As discussed above in section 2, the small particle size, as well as structural disorder in the small particles (dia. $\sim 200 \text{ \AA}$), activates the D-band Raman scattering near 1350 cm^{-1} .

Small diameter, *single-wall* nanotubes have been synthesized with metal catalysts by maintaining a dc arc (30 V, 95 A) between two electrodes in ~ 300 Torr of He gas.[21,22] The metal catalyst (cobalt[22] or

nickel and iron[21]) is introduced into the arc synthesis as a mixture of graphite and pure metal powders pressed into a hole bored in the center of the graphite anode. The cathode is translated to maintain a fixed gap and stable current as the anode is vaporized in a helium atmosphere. In the case of nickel and iron, methane is added to the otherwise inert helium atmosphere. Nanotubes are found in carbonaceous material condensed on the water-cooled walls and also in cobweb-like structures that form throughout the arc chamber. Bright-field TEM images ($100,000\times$) of the Co-catalyzed, arc-derived carbon material reveal numerous narrow-diameter single-wall nanotubes and small Co particles with diameters in the range 10–50 nm surrounded by a thick ($\sim 50 \text{ nm}$) carbon coating[27].

4.2 Raman scattering from nested carbon nanotubes

Several Raman studies have been carried out on *nested* nanotubes[23–26]. The first report was by Hiura *et al.* [23], who observed a strong first-order band at 1574 cm^{-1} and a weaker, broader D-band at 1346

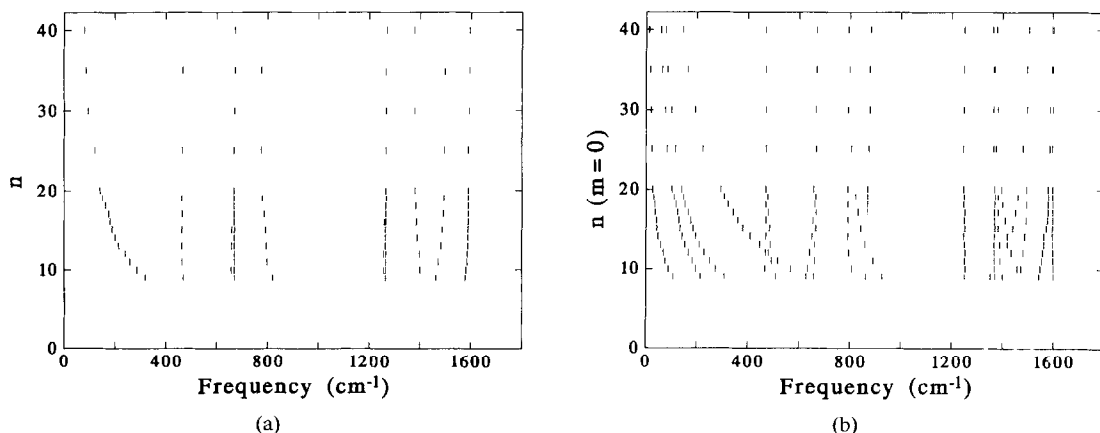


Fig. 6. Diameter dependence of the first order (a) IR-active and, (b) Raman-active mode frequencies for "zig-zag" nanotubes.

cm^{-1} . The feature at 1574 cm^{-1} is strongly downshifted relative to the 1582 cm^{-1} mode observed in HOPG, possibly a result of curvature and closure of the tube wall. These authors also observe reasonably sharp second order Raman bands at 2687 cm^{-1} and 2455 cm^{-1} .

Other Raman studies of cathode core material grown by the same method, and also shown by TEM to contain nested nanotubes as well as carbon nanoparticles, have reported slightly different results (Figs. 7, 8). Chandrabhas *et al.* [24] report a first-order Raman spectrum, Fig. 7, curve (b), for the cathode core material similar to that of polycrystalline graphite, Fig. 7, curve (a), with a strong, disorder-broadened band at 1583 cm^{-1} , and a weaker, D-band at 1353 cm^{-1} . For comparison, the Raman spectrum for the outer shell material from the cathode, Fig. 7, curve (c), is also shown. The spectrum for the outer shell exhibits the character of a disordered sp^2 carbon (i.e., carbon black or glassy carbon, c.f. Figs. 2d and 2e). Additionally, weak Raman features were observed at very low frequencies, 49 cm^{-1} and 58 cm^{-1} , which are upshifted, respectively, by 7 cm^{-1} and 16 cm^{-1} from the $E_{2g}^{(1)}$ shear mode observed in graphite at 42 cm^{-1} (Fig. 1d). The authors attributed this upshifting to defects in the tubule walls, such as inclusion of pentagons and heptagons. However, two shear modes are consistent with the cylindrical symmetry, as the planar $E_{2g}^{(1)}$ shear modes should split into a rotary and a telescope mode, as shown schematically in Fig. 9. The second-order Raman spectrum of Chandrabhas *et al.*, Fig. 8, curve (b), shows a strong line at 2709 cm^{-1} downshifted and narrower than its counterpart in polycrystalline graphite at 2716 cm^{-1} , Fig. 8, curve (a). Thus, although the first-order mode (1583 cm^{-1}) in the core material is broader than in graphite, indicating some disorder in the tubule wall, the 2709 cm^{-1} feature is actually narrower than its graphitic counterpart, suggesting a reduction in the phonon dispersion in tubules relative to that in graphite.

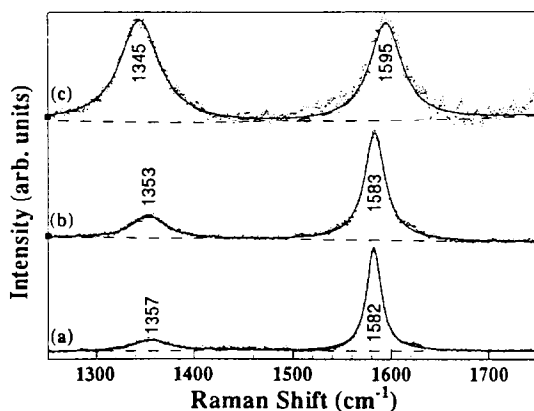


Fig. 7. First-order Raman spectra of (a) graphite, (b) inner core material containing nested nanotubes, (c) outer shell of carbonaceous cathode deposit (after ref. [24]).

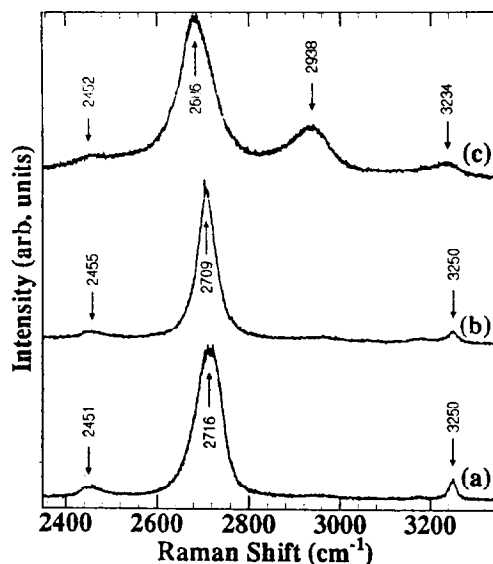


Fig. 8. Second-order Raman spectra of (a) graphite, (b) inner core material containing nested nanotubes, (c) outer shell of cathode (after ref. [24]).

Kastner *et al.* [25] also reported Raman spectra of cathode core material containing nested tubules. The spectral features were all identified with tubules, including weak D-band scattering for which the laser excitation frequency dependence was studied. The authors attribute some of the D-band scattering to curvature in the tube walls. As discussed above, Bacsa *et al.* [26] reported recently the results of Raman studies on oxidatively purified tubes. Their spectrum is similar to that of Hiura *et al.* [23], in that it shows very weak D-band scattering. Values for the frequencies of all the first- and second-order Raman features reported for these nested tubule studies are also collected in Table 1.

4.3 Small diameter single-wall nanotubes

Recently, Bethune *et al.* [22] reported that single-wall carbon nanotubes with diameters approaching the diameter of a C_{60} fullerene (7 \AA) are produced when cobalt is added to the dc arc plasma, as observed in TEM. Concurrently, Iijima *et al.* [21] described a similar route incorporating iron, methane, and argon in the dc arc plasma. These single-wall tubule samples provided the prospect of observing experimentally the many intriguing properties predicted theoretically for small-diameter carbon nanotubes.

Holden *et al.* [27] reported the first Raman results on nanotubes produced from a Co-catalyzed carbon arc. Thread-like material removed from the chamber was encapsulated in a Pyrex ampoule in ~ 500 Torr of He gas for Raman scattering measurements. Sharp first-order lines were observed at 1566 and 1592 cm^{-1} and second-order lines at 2681 and 3180 cm^{-1} , but *only when cobalt was present in the core of the anode*. These sharp lines had not been observed previously in

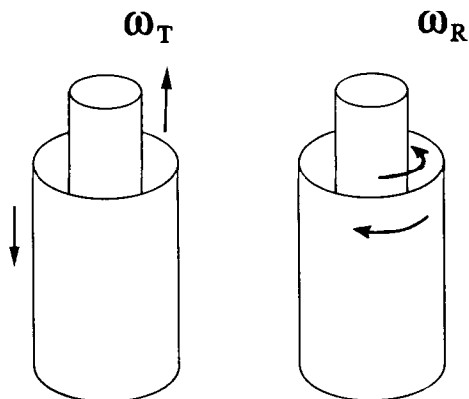


Fig. 9. Schematic view of cylindrical shear modes for a nested tubule: telescope mode (ω_T) and rotary mode (ω_R).

carbonaceous materials and were assigned to single-wall carbon nanotubes. A representative spectrum, $I_{Co}(\omega)$, is shown in Fig. 10a for *Co-catalyzed, arc-derived carbons* (solid line) over the frequency range 300–3300 cm^{-1} . This sample also contained a large fraction of other sp^2 carbonaceous material, so a subtraction scheme was devised to remove the spectral contributions from these carbons. The dashed line in the figure represents the spectrum $I_0(\omega)$ obtained from thread-like carbon removed from the chamber when cobalt was not present in the carbon anode. All other sample preparation conditions were identical to those used to prepare the Co-catalyzed carbons. $I_0(\omega)$ was scaled by a factor $\alpha = 0.85$ to superimpose with $I_{Co}(\omega)$ in the region near 1590 cm^{-1} .

Prominent in both first-order Raman spectra Fig. 10a is the broad D-band centered at 1341 cm^{-1} . Two second-order features, one at 2681 $\text{cm}^{-1} \approx 2(1341 \text{ cm}^{-1})$ and 3180 the other at $\text{cm}^{-1} \approx 2(1592 \text{ cm}^{-1})$ are apparent in the Co-catalyzed carbon. Weak features near 1460 cm^{-1} were identified with fullerenes

because they were not present after boiling the thread-like material in toluene. The overall strength and relative intensities of the sharp peaks at 1566, 1592, 2681, and 3180 cm^{-1} remained the same, implying that these features were not related to fullerenes or other toluene soluble impurities, such as polyaromatic hydrocarbons. The significant strength of the 1592 cm^{-1} line suggests that a resonant Raman scattering process may be involved [27]. Importantly, $I_0(\omega)$ shows no evidence for any of the sharp first- or second-order features and is very similar to that of Fig. 2d (disordered carbon black). Noting that these disordered sp^2 carbons likely contribute to both $I_0(\omega)$ and $I_{Co}(\omega)$, Holden *et al.* [27] compute the “difference spectrum”; $I_{diff}(\omega) = I_{Co}(\omega) - \alpha I_0(\omega)$, which is shown in Fig. 10b. $I_{diff}(\omega)$ was constructed to emphasize contributions from new carbonaceous material(s) (e.g., carbon nanotubes), which form only when Co is present in the plasma. This difference spectrum has a fairly flat baseline with sharp first-order lines at 1566 and 1592 cm^{-1} . The inset shows a Lorentzian lineshape fit to the first-order spectrum. Sharp second-order features at 2681 and 3180 cm^{-1} are also observed.

Hiura *et al.* [23] observed two Raman lines in their spectrum of *nested* carbon nanotubes at 1574 (FWHM = 23 cm^{-1}) and at 2687 cm^{-1} . It is interesting to note that their first-order peak at 1574 cm^{-1} lies between, and is more than twice as broad, as either of the two first-order lines in $I_{diff}(\omega)$ identified [27] with single-wall nanotubes. These two observations may be consistent if an inhomogeneous broadening mechanism, originating from a distribution of tubule diameters and chiralities is active. Also, the second-order feature of Hiura *et al.* [23] at 2687 cm^{-1} is slightly broader than, and upshifted from, the second-order feature at 2681 cm^{-1} in $I_{diff}(\omega)$. It should also be noted that the second-order features in $I_{diff}(\omega)$ are downshifted significantly relative to other sp^2 carbons (see Table 1).

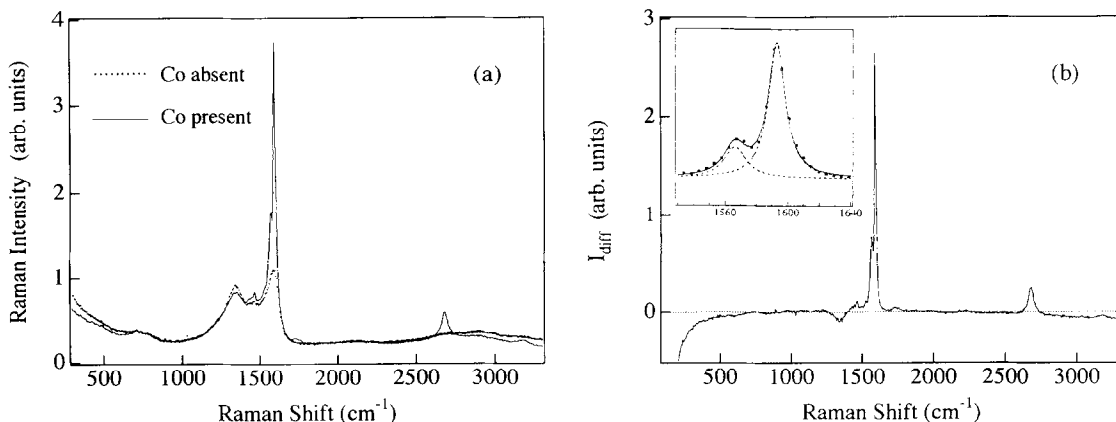


Fig. 10. (a) Raman spectra ($T = 300 \text{ K}$) of arc-derived carbons from a dc arc: cobalt was absent (dotted line) and cobalt was present (solid line) in the carbon anode, (b) the difference spectrum calculated from (a), emphasizing the contribution from Co-catalyzed nanotubes, the inset to (b) depicts a Lorentzian fit to the first-order spectrum (after ref. [27]).

In Fig. 11 we show the Raman spectrum of carbonaceous soot containing $\sim 1\text{--}2$ nm diameter, single-wall nanotubes produced from Co/Ni-catalyzed carbon plasma[28]. These samples were prepared at MER, Inc. The sharp line components in the spectrum are quite similar to that from the Co-catalyzed carbons. Sharp, first-order peaks at 1568 cm^{-1} and 1594 cm^{-1} , and second-order peaks at $\sim 2680\text{ cm}^{-1}$ and $\sim 3180\text{ cm}^{-1}$ are observed, and identified with single-wall nanotubes. Superimposed on this spectrum is the contribution from disordered sp^2 carbon. A narrowed, disorder-induced D-band and an increased intensity in the second-order features of this sample indicate that these impurity carbons have been partially graphitized (i.e., compare the spectrum of carbon black prepared at 850°C , Fig. 1d, to that which has been heat treated at 2820°C , Fig. 1c).

5. CONCLUSIONS

It is instructive to compare results from the various Raman scattering studies discussed in sections 4.2 (nested nanotubes) and 4.3 (single-wall nanotubes). Ignoring small changes in eigenmode frequencies, due to curvature of the tube walls, and the weak van der Waals interaction between nested nanotubes, the zone-folding model should provide reasonable predictions for trends in the Raman data. Of course, the low-frequency telescope and rotary, shear-type modes anticipated in the range $\sim 30\text{--}50\text{ cm}^{-1}$ (Fig. 9) are outside the scope of the single sheet, zone-folding model.

Considering all the spectra from nested tubule samples first, it is clear from Table 1 that the data from four different research groups are in reasonable agreement. The spectral features identified with tubules appear very similar to that of graphite with sample-dependent variation in the intensity in the "D" (disorder-induced) band near 1350 cm^{-1} and also in the second-order features associated with the D-band (i.e., $2 \times D \approx 2722\text{ cm}^{-1}$) and $E_{2g}^{(2)} + D \approx 2950\text{ cm}^{-1}$. Sample-dependent D-band scattering may stem from the relative admixture of nanoparticles and nanotubes, or defects in the nanotube wall.

The zone-folding model calculations predict ~ 14 new, first-order Raman-active modes activated by the closing of the graphene sheet into a tube. The Raman activity (i.e., spectral strength) of these additional modes has not been addressed theoretically, and it must be a function of tubule diameter, decreasing with increasing tubule diameter. Thus, although numerous first-order modes are predicted by group theoretical arguments in the range from 200 to 1600 cm^{-1} , their Raman activity may be too small to be observed in the larger diameter, nested nanotube samples. As reported by Bacsa *et al.* [26], their nested tubule diameter distribution peaked near 10 nm and extended from $\sim 8\text{--}40\text{ nm}$, and the Raman spectrum for this closely resembled graphite. No zone-folded modes were resolved in their study. Importantly, they oxidatively purified their sample to enhance the concentration of tubules and observed no significant change in the spectrum other

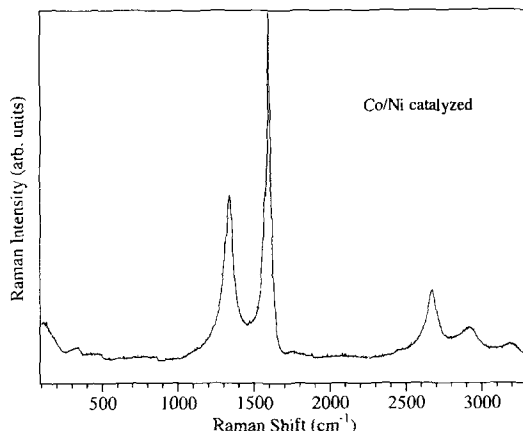


Fig. 11. Raman spectrum ($T = 300\text{ K}$) of arc-derived carbons containing single-wall nanotubes generated in a Ni/Co-catalyzed dc arc (after ref. [42]).

than a new peak at $\sim 2900\text{ cm}^{-1}$, which they attributed to C-H stretching modes.² We can, then, be reasonably certain that their spectrum is primarily associated with large-diameter carbon nanotubes, and not nanoparticles. In addition, they observed a very weak D-band, suggesting the tubes were fairly defect-free or that D-band scattering stems only from nanoparticles or other disordered sp^2 carbons. We can conclude that tubules with diameters greater than $\sim 8\text{ nm}$ will have a Raman spectrum very similar to graphite, and that the Raman activity for the zone-folded modes may be too small to be detected experimentally. The tube diameter distributions in two other nested-tube studies[24,25] reviewed here (see Table 1) were somewhat larger than reported by Bacsa *et al.* [26]. In both these cases[24,25], the Raman spectra were very similar to disordered graphite. Interestingly, the spectra of Hiura *et al.* [23], although appearing nearly identical to other nested tubule spectra, exhibit a significantly lower first-order mode frequency (1574 cm^{-1}).

Metal-catalyzed, single-wall tubes, by comparison, are found by high-resolution TEM to have much smaller diameters (1 to 2 nm)[44], which is in the range where the zone-folding model predicts noticeable mode frequency dependence on tubule diameter[27]. This is the case for the single-wall tube samples whose data appear in columns 4 and 5 in Table 1. Sharp line contributions to the Raman spectra for single-wall tubule samples produced by Co[27] and Ni/Co[28] are also found, and they exhibit frequencies in very good agreement with one another. Using the difference spectrum of Holden *et al.* [27] to enhance the contribution from the nanotubes results in the first- and second-order frequencies found in column 4 of Table 1. As can be seen in the table, the single-wall tube frequencies are noticeably different from those reported for larger diameter (nested) tubules. For example, in

²The source of the hydrogen in their air treatment is not mentioned; presumably, it is from H_2O in the air.

first-order, sharp modes are observed[27] at 1566 and 1594 cm^{-1} , one downshifted and one upshifted from the value of the E_{2g}^2 mode at 1582 cm^{-1} for graphite. From zone-folding results, the near degeneracy of the highest frequency Raman mode is removed with decreasing tubule diameter; the mode frequencies spread, some upshifting and some downshifting relative to their common large-diameter values. Thus, the observation of the sharp modes at 1566 cm^{-1} and 1592 cm^{-1} for 1–2 nm tubules is consistent with this theoretical result.

Finally, in second order, the Raman feature at $\sim 3180 \text{ cm}^{-1}$ observed in Co- and Ni/Co-catalyzed single-wall nanotube corresponds to a significantly downshifted $2 \times E_{2g}'$ mode, where E_{2g}' represents the mid-zone (see Figs. 1a and 1b) frequency maximum of the uppermost optic branch seen in graphite at 3250 cm^{-1} .

Acknowledgement—We gratefully acknowledge valuable discussions with M. S. Dresselhaus and G. Dresselhaus, and Y. F. Balkis for help with computations. One of the authors (RAJ) acknowledges AFOSR Grant No. F49620-92-J-0401. The other author (PCE) acknowledges support from University of Kentucky Center for Applied Energy Research and the NSF Grant No. EHR-91-08764.

REFERENCES

- R. A. Jishi, L. Venkataraman, M. S. Dresselhaus, and G. Dresselhaus, *Chem. Phys. Lett.* **209**, 77 (1993).
- R. A. Jishi, L. Venkataraman, M. S. Dresselhaus, and G. Dresselhaus, *Chem. Phys. Lett.* **209**, 77 (1993).
- R. A. Jishi, M. S. Dresselhaus, and G. Dresselhaus, *Phys. Rev. B* **47**, 16671 (1993).
- E. G. Gal'pern, I. V. Stankevich, A. L. Christyakov, and L. A. Chernozatonskii, *JETP Lett. (Pis'ma Zh. Eksp. Teor.)* **55**, 483 (1992).
- N. Hamada, S.-I. Sawada, and A. Oshiyama, *Phys. Rev. Lett.* **68**, 1579 (1992).
- R. Saito, G. Dresselhaus, and M. S. Dresselhaus, *Chem. Phys. Lett.* **195**, 537 (1992).
- J. W. Mintmire, B. I. Dunalp, and C. T. White, *Phys. Rev. Lett.* **68**, 631 (1992).
- K. Harigaya, *Chem. Phys. Lett.* **189**, 79 (1992).
- K. Tanaka *et al.*, *Phys. Lett.* **A164**, 221 (1992).
- J. W. Mintmire, D. H. Robertson, and C. T. White, *J. Phys. Chem. Solids* **54**, 1835 (1993).
- P. W. Fowler, *J. Phys. Chem. Solids* **54**, 1825 (1993).
- C. T. White, D. H. Robertson, and J. W. Mintmire, *Phys. Rev. B* **47**, 5485 (1993).
- T. W. Ebbesen and P. M. Ajayan, *Nature (London)* **358**, 220 (1992).
- T. W. Ebbesen *et al.*, *Chem. Phys. Lett.* **209**, 83 (1993).
- H. M. Duan and J. T. McKinnon, *J. Phys. Chem.* **49**, 12815 (1994).
- M. Endo, Ph.D. thesis (in French), University of Orleans, Orleans, France (1975).
- M. Endo, Ph.D. thesis (in Japanese), Nagoya University, Japan (1978).
- M. Endo and H. W. Kroto, *J. Phys. Chem.* **96**, 6941 (1992).
- X. F. Zhang *et al.*, *J. Cryst. Growth* **130**, 368 (1993).
- S. Amelinckx *et al.*, personal communication.
- S. Iijima and T. Ichihashi, *Nature (London)* **363**, 603 (1993).
- D. S. Bethune *et al.*, *Nature (London)* **363**, 605 (1993).
- H. Hiura, T. W. Ebbesen, K. Tanigaki, and H. Takahashi, *Chem. Phys. Lett.* **202**, 509 (1993).
- N. Chandrabhas *et al.*, *PRAMA-J. Physics* **42**, 375 (1994).
- J. Kastner *et al.*, *Chem. Phys. Lett.* **221**, 53 (1994).
- W. S. Bacsá, D. U. A., Châtelain, and W. A. de Heer, *Phys. Rev. B* **50**, 15473 (1994).
- J. M. Holden *et al.*, *Chem. Phys. Lett.* **220**, 186 (1994).
- J. M. Holden, R. A. Loufity, and P. C. Eklund (unpublished).
- P. Lespade, R. Al-Jishi, and M. S. Dresselhaus, *Carbon* **20**, 427 (1982).
- A. W. Moore, In *Chemistry and Physics of Carbon* (Edited by P. L. Walker and P. A. Thrower), Vol. 11, p. 69, Marcel Dekker, New York (1973).
- L. J. Brillson, E. Burnstein, A. A. Maradudin, and T. Stark, In *Proceedings of the International Conference on Semimetals and Narrow Gap Semiconductors* (Edited by D. L. Carter and R. T. Bate), p. 187, Pergamon Press, New York (1971).
- Y. Wang, D. C. Alsmeyer, and R. L. McCreery, *Chem. Matter.* **2**, 557 (1990).
- F. Tunistra and J. L. Koenig, *J. Chem. Phys.* **53**, 1126 (1970).
- X.-X. Bi *et al.*, *J. Mat. Res.* (1994), submitted.
- J. C. Charlier, Ph.D. thesis (unpublished), Universite Catholique De Louvain (1994).
- W. S. Bacsá, W. A. de Heer, D. Ugarte, and A. Châtelain, *Chem. Phys. Lett.* **211**, 346 (1993).
- S. Iijima, *Nature (London)* **354**, 56 (1991).
- S. Iijima, T. Ichihashi, and Y. Ando, *Nature (London)* **356**, 776 (1992).
- P. M. Ajayan and S. Iijima, *Nature (London)* **361**, 333 (1993).
- L. S. K. Pang, J. D. Saxby, and S. P. Chatfield, *J. Phys. Chem.* **97**, 6941 (1993).
- S. C. Tsang, P. J. F. Harris, and M. L. H. Green, *Nature (London)* **362**, 520 (1993).
- P. M. Ajayan *et al.*, *Nature (London)* **362**, 522 (1993).
- T. W. Ebbesen, P. M. Ajayan, H. Hiura, and K. Tanigaki, *Nature (London)* **367**, 519 (1994).
- C. H. Kiang *et al.*, *J. Phys. Chem.* **98**, 6612 (1994).